Synchronization of Large Josephson-Junction Arrays by Traveling Electromagnetic Waves

M. A. Galin,[1,2,*] E. A. Borodianskyi,[2] V. V. Kurin,[1] I. A. Shereshevskiy,[1] N. K. Vdovicheva,[1]
V. M. Krasnov,[2] and A. M. Klushin[1]

[1]*Institute for Physics of Microstructures RAS, 603950 Nizhny Novgorod, Russia*
[2]*Department of Physics, Stockholm University, AlbaNova University Center, SE-10691 Stockholm, Sweden*

Mutual synchronization of many Josephson junctions is required for superradiant enhancement of the emission power. However, the larger the junction array is, the more difficult is the synchronization, especially when the array size becomes much larger than the emitted wavelength. Here, we study experimentally Josephson emission from such larger-than-the-wavelength Nb/NbSi/Nb junction arrays. For one of the arrays we observe a clear superradiant enhancement of emission above a threshold number of active junctions. The arrays exhibit strong geometrical resonances, seen as steps in current-voltage characteristics. However, radiation patterns of the arrays have forward-backward asymmetry, which is inconsistent with the solely geometrical resonance (standing-wave) mechanism of synchronization. We argue that the asymmetry provides evidence for an alternative mechanism of synchronization mediated by unidirectional traveling-wave propagation along the array (such as a surface plasmon). In this case, emission occurs predominantly in the direction of propagation of the traveling wave. Our conclusions are supported by numerical modeling of Josephson traveling-wave antenna. We argue that such a nonresonant mechanism of synchronization opens a possibility for phase locking of very large arrays of oscillators.

I. INTRODUCTION

The Josephson effect can be used for the generation of high-frequency electromagnetic radiation [1,2]. The frequency is limited only by the superconducting energy gap. For low-T_c superconductors the frequency is in the sub-THz range [2] and for high-T_c superconductors it can be up to approximately 20 THz [3,4]. The emission power from a single Josephson junction (JJ) is small. It can be enhanced in a superradiant manner using JJ arrays, containing many, $N \gg 1$, synchronized junctions [5–15]. Synchronization is usually mediated by some resonant electromagnetic mode, such as a cavity mode (standing electromagnetic wave) either in the external cavity [5], in the junction [6,16–18], or in the dielectric substrate [7]. For achieving a practically important mW level of emission power very large arrays containing $N \sim 10^4$–10^5 JJs would be needed. Taking into account the attainable integration density, such arrays would have a typical size of $L \sim 1$ cm, which is significantly larger than the wavelength λ even at sub-THz frequencies.

The larger the array is, the more difficult is the synchronization. This is caused by the spread in junction parameters, which statistically increases with N, unequal environmental conditions for inner and outer JJs, and large

phase delays along the array. Recently, it was suggested [19] that in such a nonresonant case the synchronization can be mediated by a unidirectional traveling wave along the array, qualitatively similar to the operation of a traveling-wave (Beverage) antenna [20]. The main fingerprint of the traveling-wave regime is a strong forward-backward asymmetry of the radiation pattern with the majority of power emitted in the propagation direction of the traveling wave. This is qualitatively different from the resonant, standing-wave case, which per definition has a symmetric radiation pattern. Thus, the shape of the radiation pattern allows a clear distinction of the two scenarios.

Here, we study angular dependence of electromagnetic wave emission from large Nb/NbSi/Nb JJ arrays with $N \sim 10^4$ JJs. The overall size of arrays approximately 0.5×0.5 cm is several times larger than the emitted wavelength. We obtain evidence for superradiant emission from one of the arrays showing a rapid enhancement of the emission power above a threshold number of active JJs. The current-voltage characteristics of the arrays exhibit profound steps, indicating the presence of strong cavity mode resonances. However, measured radiation patterns exhibit significant forward-backward asymmetry, inconsistent with solely the standing-wave mechanism of synchronization of the arrays. We argue that the observed asymmetry is due to the involvement of the alternative traveling-wave mechanism of synchronization. In the end,

*galin@ipmras.ru
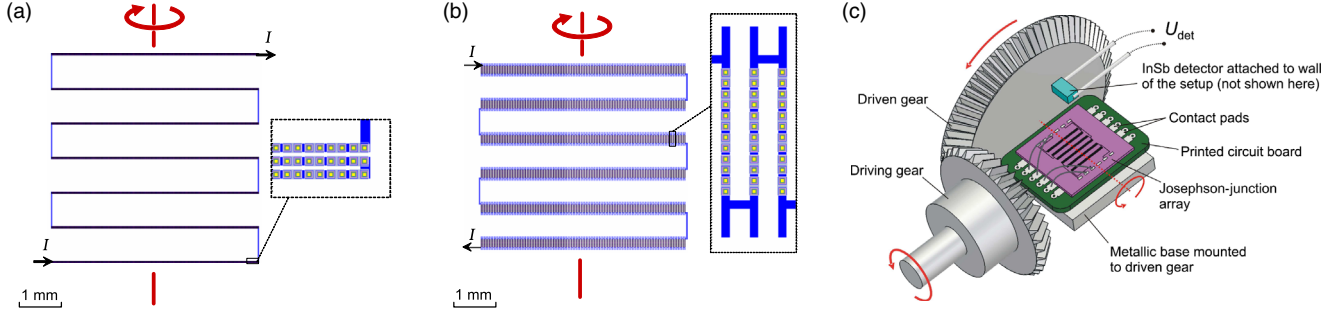
FIG. 1. Layouts of linear (a) and meander (b) JJ arrays. Arrows I denote input and output current contacts. Red lines indicate rotation axes in the detection experiment. (c) Measurement setup for studying angular dependence of the emission from arrays using the InSb detector. The shown array-detector orientation corresponds to the angle $\alpha = 90°$. Arrows indicate the rotation direction for the decremental angle.

we present numerical simulations of the Josephson traveling-wave antenna supporting our conclusions. We argue that this mechanism of synchronization opens a possibility for phase locking of very large junction arrays, which is important for the enhancement of the output power from Josephson-junction arrays, as well as for other types of coupled coherent oscillators [21].

II. EXPERIMENTAL

We study two Nb/NbSi/Nb junction arrays with different arrangements of JJs, as shown in Figs. 1(a) and 1(b). The first, "linear" array, see Fig. 1(a), consists of seven long linear subarrays (longer than the wavelength), each containing three lines connected in series. Every line contains 332 JJs. The total number of junctions in the linear array is $N_1 = 332 \times 3 \times 7 = 6972$. The second, "meander" array, see Fig. 1(b), consists of six subarrays with short lines meandering in the direction perpendicular to the long side of the array. Each subarray contains 125 short lines with 12 JJs per line. The total number of junctions in the meander array is $N_2 = 12 \times 125 \times 6 = 9000$. For both arrays JJs have similar areas 8×8 μm and the separation between neighbor JJs is 7 μm. The overall size of both arrays is approximately 0.5×0.5 cm. The arrays are made on top of silicon substrates 1×1 cm with the thickness 0.38 mm. Details about array fabrication and characterization can be found in Refs. [22] and [8], respectively.

Electromagnetic waves are detected using a high-purity *n*-doped InSb bolometer [23]. The detector is calibrated using a backward-wave oscillator in the frequency range 100–118 GHz. We measure either a dc-voltage response U_{det} at a fixed dc-bias current, or a zero-bias resistance R_{det} with a small ac current through the detector. The calibrated responsivity at 4.2 K is approximately 300 V/W and 5×10^6 Ω/W for dc- and ac-measurement schemes, respectively.

Measurements are performed in a closed-cycle cryostat with a sample-in-gas cooling and the base $T = 1.8$ K. Arrays are mounted on a rotatable sample holder, as

depicted in Fig. 1(c). The substrate holder (printed circuit board) is sitting on a rotation table (metallic base) attached to the driven gear. The rotation axis of the sample coincides with the rotation axis of the driven gear. Arrows indicate the direction of sample rotation in the decremental angle direction. The InSb detector is permanently fixed to the holder (not shown in the figure) and not rotating. Only the sample rotates while the detector is fixed during the measurements. The average distance from the middle of the sample to the detector is not changing upon rotation because the rotation axis coincides with the sample plane. The rotation axes for both arrays are specified in Figs. 1(a) and 1(b). The angle $\alpha = 90°$ corresponds to the detector face-to-face on top of the array, as shown in Fig. 1(c), and $\alpha = 0°$ to the detector at the sliding angle with respect to the array. The absolute accuracy of array-detector alignment is several degrees. The relative accuracy of the rotator stage is 0.02°. The detector is located at approximately 1 cm from the geometrical center of the array. The Fresnel parameter for such an emitter-detector configuration is near 1. That is not enough for true far-field measurements but it, nevertheless, allows a qualitative estimation of the radiation pattern symmetry.

III. RESULTS

Figure 2 shows current-voltage characteristics (IVCs) of (a)–(c) the linear and (d)–(f) the meander arrays recorded at different orientations of the sample. Colors represent the detected emission power (dc-voltage response of the detector), indicated by color scales to the right. Upon increasing the bias current above the critical current $I_c \sim$ 3 mA almost all JJs switch simultaneously into the resistive state. Several pronounced steps in the IVCs appear at $U \sim 2$ V. Those steps were studied in Ref. [8] and were attributed to standing-wave resonances in the line parts of the arrays. From the color scale it is seen that for the linear array the maximum emission occurs at the steps, as shown in the inset in Fig. 2(c). However, for the meander array the maximum emission occurs outside the step; see the inset in
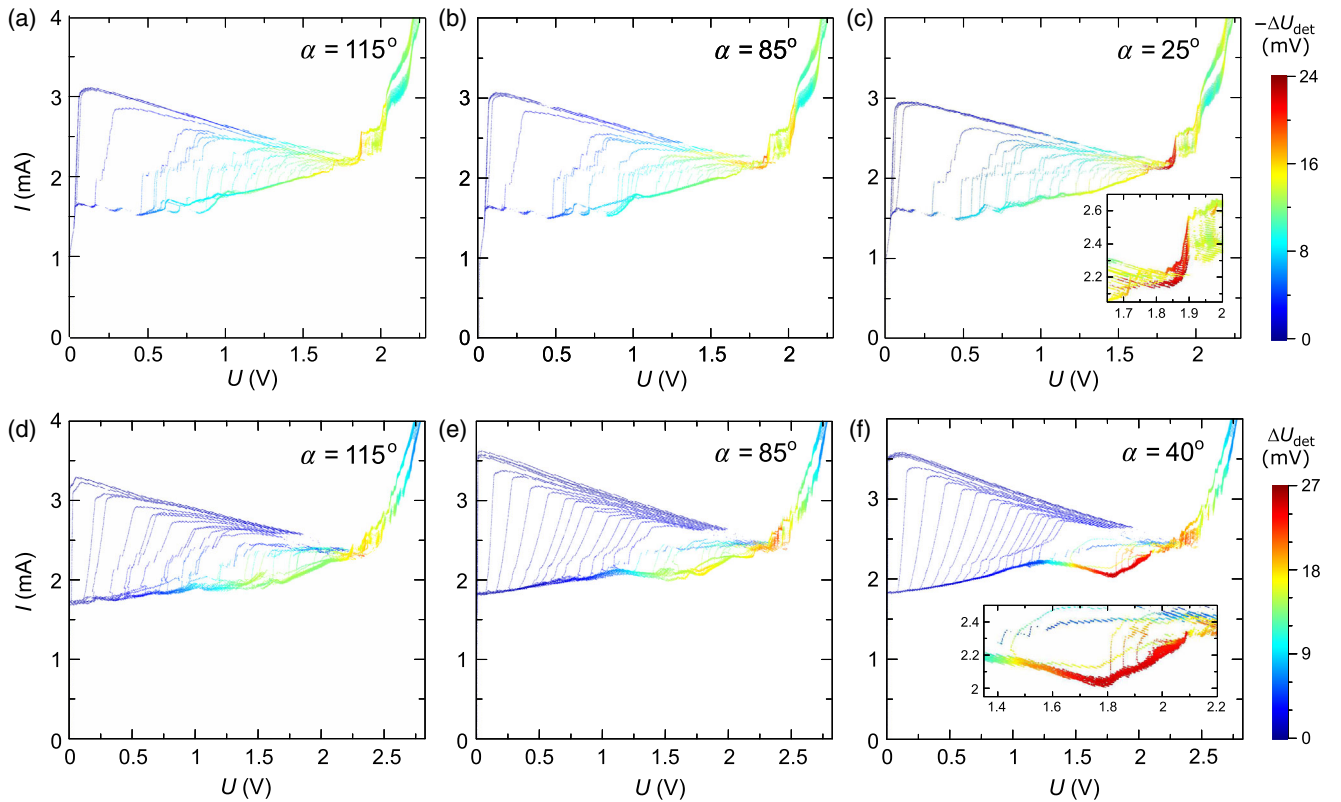
FIG. 2.   Current-voltage characteristics of (a)–(c) the linear and (d)–(f) the meander arrays. The IVCs in panels (a) and (d) correspond to the backward side $\alpha > 90°$ with a small emission, in (b) and (e) close to the normal orientation with the detector face-to-face on top of the array, and in (c) and (f) to emission maxima in the forward ($\alpha < 90°$) direction. Colors represent the detected power (dc-detector response), indicated by color scales in the right panels. Multiple inner sub-branches in the IVCs are obtained by repeated back-and-forth sweeping starting from different points at the returning side of the IVCs and correspond to a different number of active (oscillating) junctions in the resistive state.

Fig. 2(f). This suggests that standing waves play a more prominent role in the emitted electromagnetic field for the linear, than for the meander array.

Upon decreasing the bias current the array is retrapped back to the superconducting state at a lower current approximately 1.5 mA. This leads to the appearance of a hysteresis in the IVCs. We note that single Nb/NbSi/Nb junctions do not exhibit either significant hysteresis or resonant steps in the IVCs [22]. Therefore, individual junctions are overdamped (have a small capacitance) and the observed hysteresis in our arrays is predominantly of a thermal origin and is caused by a significant total dissipation power approximately 10 mW at the highest bias.

Unlike switching, the retrapping is more gradual. A closer inspection reveals that the retrapping branch of the IVC consists of many inner sub-branches, corresponding to sequential retrapping of small groups of JJs. Most likely, this is due to temperature gradients inside the array: outer JJs located closer to the edges of the arrays are cooler and retrap at a larger current than inner JJs situated closer to the hotter middle parts of the arrays. The hysteresis persists even at inner branches. Therefore, if the bias direction is reversed at the retrapping side of the IVC, i.e., if we start to

increase the current, an another sub-branch is recorded. The IVCs in Fig. 2 are measured in such a way by repeated back-and-forth sweeping of the bias current starting from different points at the retrapping side of the IVC. This allows the observation of numerous inner sub-branches in the IVCs. At each of the sub-branches a certain group of junctions remains in the superconducting state and is passive (do not emit), while the rest of the junctions are in the resistive state (active). The larger the number of active junctions is, the larger is the total voltage of the sub-branch. Thus, the presence of thermal hysteresis and inner sub-branches in the IVCs allows analysis of the emission at different numbers of active junctions, which is approximately proportional to the voltage at the particular sub-branch.

From Fig. 2 it can be seen that the IVCs of both arrays do not change appreciably upon rotation of the array with respect to the detector. A slightly different set of sub-branches in the IVCs depends mostly on the current-sweeping history due to the presence of hysteresis in the IVCs. However, the detected power does change, reflecting the angular dependence of the radiation pattern. We estimate the maximum detected power 80
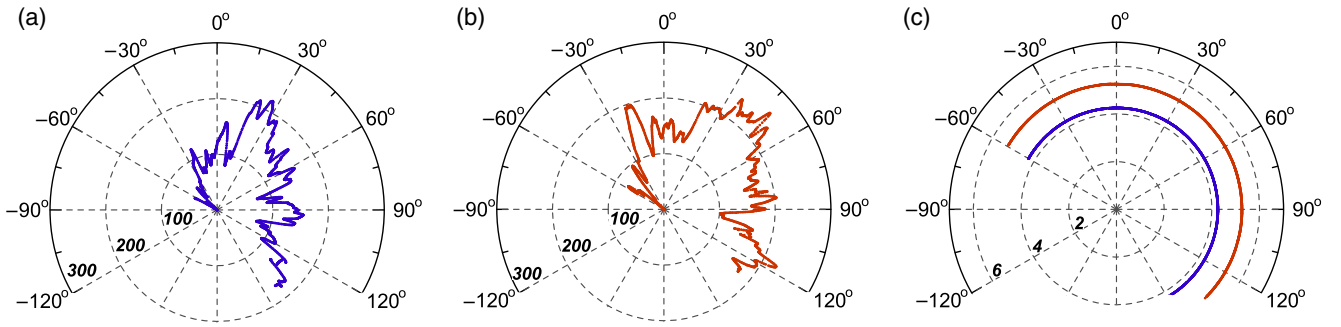
FIG. 3. Measured radiation patterns, angular dependence of the ac-detected signal $-\Delta R_{det}$ (ohm) for (a) linear and (b) meander arrays. Note a forward ($\alpha < 90°$) and backward ($\alpha < 90°$) asymmetry of the diagrams, which is more visible for the meander array. (c) Angular dependence of the total consumed power $P = IU$ (mW) at corresponding bias points for linear (blue) and meander (red line) arrays. Constancy of P demonstrates stability of the bias points.

and approximately 90 μW for linear and meander arrays, respectively.

During angular-dependent measurements it is necessary to have a stable bias point. Upon measurements of the radiation patterns, we put special attention on the analysis of such stability for different bias points. Generally, metastable points at inner branches are not stable because they can sporadically switch to another state. Also, the ends of the resonant steps in IVCs with a maximum emission are not particularly stable because the system can be prematurely driven out of the resonance by thermal fluctuations and noise. At such metastable points the angular dependence is irreproducible and exhibits history-dependent hysteresis. Therefore, for angular measurements we have specifically chosen the bias point close to the middle of the emitting step in the IVC—which are stable. The presented radiation patterns are fully reproducible and were measured many times with the same result. We are confident that such data represent reproducible angular dependence of the emission rather than irreproducible fluctuations of the bias point.

Figures 3(a) and 3(b) show measured angular dependencies of emission (radiation patterns) for (a) linear and (b) meander arrays. They represent changes $-\Delta R_{det}$ relative to the case with no emission (unbiased array). Measurements are made at $U_1 = 1.879$ V for the linear and $U_2 = 2.223$ V for the meander arrays, corresponding to oscillation frequencies $f_1 = 130.2$ GHz and $f_2 = 119.3$ GHz, respectively. High stability of selected bias points U_1, U_2 is demonstrated in Fig. 3(c), which shows the total consumed power measured simultaneously with the corresponding angular-dependent measurements. The maxima of emission occur at $\alpha \simeq 25°$ and $40°$ for linear and meander arrays, correspondingly. It is seen that both arrays have complex multilobe radiation patterns with a visible asymmetry in emission between forward ($\alpha < 90°$) and backward ($\alpha > 90°$) directions [24].

Observation of forward-backward asymmetry of emission is the main result of our work. As mentioned above, such asymmetry is inconsistent with the resonant mechanism of synchronization of the arrays by standing waves because standing waves per definition should have forward-backward symmetric radiation patterns. Furthermore, the asymmetry is more pronounced for the meander array, for which the maximum emission occurs outside the standing-wave resonant step in the IVC; see the inset in Fig. 2(f). As we will argue below, the observed asymmetry is consistent with a nonresonant mechanism of synchronization of the arrays by a traveling wave [19].

We have the following arguments against an artificial nature of the observed radiation pattern asymmetry: (1) the experimental setup is symmetric and should not introduce major asymmetry. (2) The two studied arrays, with similar overall dimensions, show significantly different radiation patterns and asymmetry. The linear array emits at the step in the IVC, i.e., at the standing-wave resonance, and has a more symmetric radiation pattern, while the meander array emits outside the step and has a more asymmetric radiation pattern. (3) The total dc power in the arrays does not change upon rotation, see Fig. 3(c). We conclude that both arrays have standing and traveling waves, but in the meander array the traveling wave is more profound. This difference clearly shows that the observed asymmetry is not an artifact of the setup (which is identical for both arrays), but reflects properties of the actual radiation patterns.

IV. NUMERICAL MODELING OF JOSEPHSON TRAVELING-WAVE ANTENNA

As suggested recently by some of us [8,19], large JJ arrays may act as Josephson traveling-wave antennas. In this case, the unidirectional propagating wave imprints the corresponding phase distribution along the array and, thus, facilitates coherent emission. This is similar to the operation of the well-known Beverage antenna [20]. Traveling-wave antennas have asymmetric radiation patterns with a maximum in the direction of propagation of the wave at an angle $\alpha = \arccos h/k$, where h is the wave number of
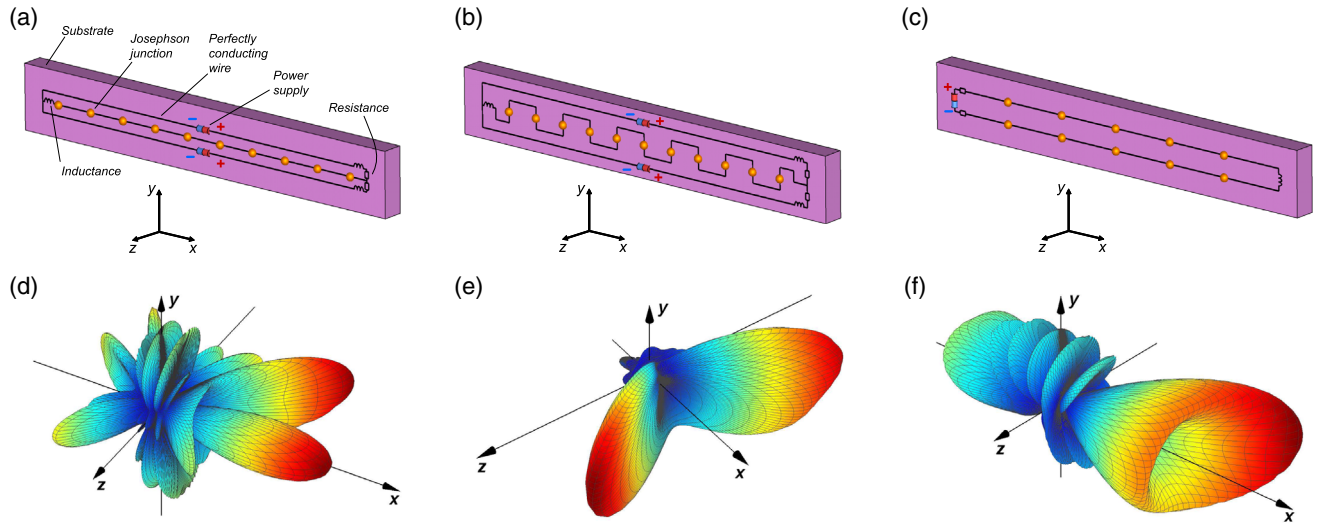
FIG. 4.   The models of the linear (a), meander (b), and twin (c) Josephson-junction arrays which are similar to the Beverage antenna. The dimensions of the substrate ($x \times y \times z$) are $8.0 \times 1.2 \times 0.4$ mm, its dielectric constant is $\varepsilon = 10$. The substrates, the shape of circuits also as the distances between Josephson junctions are displayed without distortions. The junctions are described in the RCSJ model [26] with parameters $I_c = 2.5$ mA, $R = 0.5$ Ω, $C = 0.1$ pF. (d)–(f) Simulated three-dimensional radiation patterns corresponding to the linear (d), meander (e), and twin (f) arrays. The wave propagates mainly along the x axis. A common feature of measured (Fig. 3) and simulated radiation patterns is the forward-backward asymmetry induced by the traveling wave.

current oscillations in the antenna and k is the wave number of the emitted wave in vacuum. For $h/k < 1$ it is an ordinary transverse electromagnetic wave. But for $h/k > 1$ the angle α is imaginary and the traveling wave turns to a surface plasmon at the interface between the wafer and the electrodes.

For analysis of nonlinear dynamics of the Josephson traveling-wave antennas, we develop a numerical code for solving Maxwell equations by the finite-difference time-domain method [25] in combination with self-consistent solution of junction dynamics within the resistively and capacitively shunted junction (RCSJ) model [26].

Figure 4 shows results of numerical simulations. We choose three models of JJ arrays: a straight line, Fig. 4(a), a meander line with short segments, Fig. 4(b), and a twin array with two lines connected in a Π-shaped manner, Fig. 4(c). They catch the key geometrical features of measured samples; see Figs. 1(a) and 1(b).

Simulated arrays contain 10 or 11 JJs, linear lumped passive elements and one or two voltage sources. Elements in the arrays are connected by perfectly conducting wires. The arrays are placed on dielectric substrates 8.0×1.2 mm with a thickness 0.4 mm and a dielectric permittivity $\varepsilon = 10$. We consider narrower substrates to save the calculation time. In other dimensions, length and thickness, they are almost the same as the substrates of measured arrays. Junction parameters used in simulations are critical current $I_c = 2.5$ mA, normal resistance $R_n = 0.5$ Ω, and the McCamber parameter $\beta = 0.2$. They are close to the corresponding estimated values for our Nb/NbSi/Nb junctions ($I_c \sim 3$ mA, $R_n \sim 0.1$ Ω, $\beta \sim 1$).

Different passive elements are inserted at the opposite sides of the circuits. These are resistances and inductances with the values of 25 Ω and 200 pH, respectively. These lumped elements are needed for simulating the dynamical violation of the symmetrical state that has to take place in real Josephson-junction arrays. This effect stems from instability of symmetrical solution in the symmetrical system due to fluctuations. The example of such dynamical behavior similar to the considered case is a standing-wave instability in very long lasers and annular lasers in which only the traveling mode survives due to the mode competition [27]. In the numerical simulations the fluctuations, which are the seed of unstable mode, are absent. Therefore, if special precaution has not been undertaken one may observe unstable symmetrical solution. To get rid of it, it is possible to insert lumped elements to slightly violate the symmetry of the system explicitly or use a slightly nonsymmetrical initial condition. In computer simulation we used both approaches. The internal resistance of the sources in the modeling circuits is much larger than the total resistance of JJs to provide the current biased regime.

The JJs are simulated by specific cell edges with the field dynamics determined by the following ordinary differential equations:

$$\frac{\partial \varphi_k}{\partial t} = \frac{2\pi}{\Phi_0} E_i d, \tag{1a}$$

$$I_k = Cd \frac{\partial E_i}{\partial t} + \frac{E_i d}{R} + I_c \sin \varphi. \tag{1b}$$

$$I_k = S\left(\text{rot}\vec{B} - \varepsilon_0 \frac{\partial \vec{E}}{\partial t}\right)_i . \qquad (1c)$$

Here, k is the junction number, φ_k is the Josephson phase difference, E_i ($i = x, y, z$) is the electric field components, Φ_0 is the magnetic flux quantum, d is the edge length, S is the area of the face of mesh cell, and ε_0 is the electric constant. This system of equations is solved by the semi-implicit Crank-Nicolson method [28]. The sample is surrounded by vacuum terminated at the boundaries of the calculated volume by a perfectly matched layer [29,30] that prevents reflection of electromagnetic waves.

Calculations start from an initial guess for Josephson phases and electric and magnetic fields on the grid and continue until a stationary state is reached. After that time average values of voltages and currents in JJs and Fourier amplitudes of the fields around the sample are obtained. The radiation pattern at a fixed frequency is calculated using a standard near-to-far field transformation [29]. More details about the description of the JJ array in that simulation also as the calculation procedure can be found in Ref. [31].

Numerically simulated radiation patterns for the considered arrays are shown in Figs. 4(d)–4(f). Corresponding bias currents are in the range $I = 2.5$–3.0 mA. The radiation frequencies of linear, meander, and twin JJ arrays are equal to 136.6, 143.5, and 123.2 GHz, respectively. Also, as for the measured samples, those values of frequency provide the wavelength of the current wave considerably smaller than the dimension of the circuits. The radiation power of the modeling antennas varies from 1.7 to 5.5 nW that gives the radiation efficiency near 0.1% in all cases.

From Figs. 4(d)–4(f) it is seen that irrespective of the geometry, arrays in the Josephson traveling-wave antenna regime exhibit a pronounced forward-backward asymmetry of radiation patterns with maxima in the direction of the traveling-wave propagation (positive x-axis direction). The values of directivity in the maximum power radiation for the linear, meander, and twin circuits are 4.6, 6.9, and 5.4 dBi (decibels relative to an isotropic antenna). The fine structure of the radiation patterns does depend on the geometry. The amplitude and symmetry of the side lobes is different. The radiation pattern of the linear array has two large lobes with equal amplitudes. One of them is directed strictly along the x axis that indicates a surface plasmon excited in the array. The relation $h/k > 1$ is realized in this case as mentioned in the beginning of the current chapter. For another large lobe $h/k < 1$, therefore, an ordinary traveling wave exists with the finite angular deviation from the x axis equal to $\alpha = 42°$. In the case of the meander array two similar lobes oriented almost symmetrically to the xy plane are very prominent in the radiation pattern. Those deviations from the x axis are $\alpha \sim 55°$. Such large α indicates a faster wave of current with a smaller wave number h in the meander array. The twin array has a single

but wide main lobe which is funnel shaped and slightly asymmetrical relative to the x axis. The maximum of radiated power is deviated at $\alpha = 24°$. One can notice that the radiation patterns are visually symmetrical relative to the zx plane. This condition must be necessary only for the linear array which has true planar symmetry, Fig. 4(a). The other two arrays don't have such a symmetry (for the twin array the asymmetry is only due to the nonlinearity of the Josephson junctions), Figs. 4(b) and 4(c), therefore, the corresponding radiation patterns are not required to be symmetrical in that plane.

The studied Nb/NbSi/Nb arrays are much more complex than the arrays we analyze numerically, even though we consider arrays that contain the key geometrical features of experimentally studied arrays. Therefore, the aim of those simulations is not to fit the experimental data, but rather to demonstrate that the main evidence for the traveling-wave regime, irrespective of geometry of the array, is the forward-backward asymmetry of the radiation pattern with a maximum in the traveling-wave direction. This is qualitatively consistent with the observed forward-backward asymmetry of emission from the studied large JJ arrays.

From a comparison of Figs. 1 and 3, it can be concluded that for both arrays the wave is traveling along the long side of the array, from left to right in Figs. 1(a) and 1(b). We note that this is exactly how it is predicted by numerical simulations for the corresponding linear and twin arrays, Figs. 4(d) and 4(f)—key elements of the "linear" array Fig. 1(a); and for the meander array, Fig. 4(e)—a key element of the "meander" array Fig. 1(b). Therefore, we conclude that even though numerical modeling is not a direct fit to our data, it still catches main qualitative features of our experimental data.

V. EVIDENCE FOR SUPERRADIANT EMISSION

In Figs. 5(a) and 5(b) we show experimentally detected emission power from the studied Nb/NbSi/Nb arrays (dc-voltage response of the detector) as a function of the total voltage for (a) linear and (b) meander arrays at $\alpha = 85°$ (blue) and at the angles, corresponding to emission maxima (red). Measurements are made along reverse (retrapping) branches of the IVCs. The current is swept from a large bias downward to zero. As seen from Fig. 2 the reverse branch is rather steep: a small reduction of bias current leads to a large reduction of voltage. This occurs because some junctions switch back (retrap) from the resistive into the zero-voltage state. Thus, variation of the emitted power with bias voltage is primarily due to variation of the number of oscillating junctions N, approximately proportional to voltage U. It is seen that for the linear array, Fig. 5(a), the power increases approximately linearly with increasing the number of oscillating junctions. However, for the meander array Fig. 5(b), a rapid superlinear enhancement of the emission power occurs at a
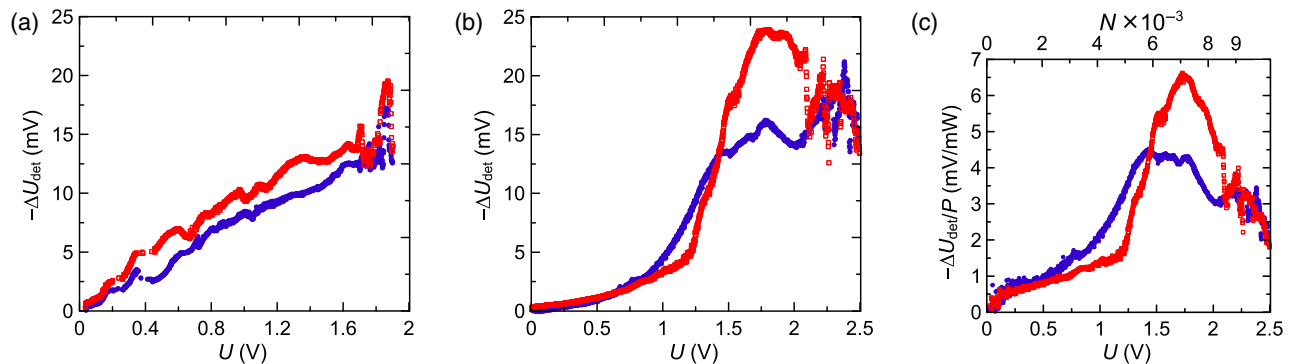
FIG. 5. Emitted electromagnetic power (dc-detector response) along the reverse branch of the IVCs of (a) linear and (b) meander arrays at $\alpha = 85°$ (blue solid circles) and at angles corresponding to the maxima of detected signal (red empty squares). (c) The signal for meander array normalized by the total consumed power in the array. The number of active junctions is indicated in the upper axis. A rapid enhancement of the emission efficacy is seen at $U \sim 1.3$–1.8 V.

threshold $U \sim 1.3$ V. We remind the reader that for the (oversimplified) case, when all the oscillating junctions are in the exactly identical state, the emission power should increase quadratically: $P_{em} \propto N^2$. More generally, $P_{em}(N)$ depends critically on the extent and the type of mutual synchronization of the array [16].

In Fig. 5(c) we replot data for the meander array, in which the detector signal is normalized by the total consumed power $P = IU$ in the array. Such a plot represents the relative emission efficacy, i.e., the ratio of the emitted power to the consumed power, which accounts for modest variations of the bias current $I(U)$. It is clearly seen how the efficacy of emission rapidly grows with increasing the number of oscillating junctions. This provides strong evidence for the occurrence of superradiant emission from the array above some threshold number of junctions, consistent with previous reports [5,32].

Finally, we want to summarize the difference in the behavior of the two studied arrays: the linear array with the $N_1 = 6972$ and the meander array with the $N_2 = 9000$ junctions.

(i) Both arrays exhibit profound standing-wave resonances, but only in the linear array the emission maxima occur at the resonant steps in the IVC, see the inset in Fig. 2(c), while in the meander array the maxima do not correspond to the steps, see the inset in Fig. 2(f). For the meander array the emission power does have secondary maxima at resonant steps at $U \simeq 2.2$ and 2.4 V, as seen from Figs. 2(f) and 5(b), but with a significantly lower efficacy, see Fig. 5(c).

(ii) The radiation patterns of emission for both arrays exhibit forward-backward asymmetry. However, it is relatively small for the linear array and more visible for the meander array.

(iii) The meander array exhibits clear evidence for the nonlinear enhancement of the emission power with increasing the number of active junctions, indicating that this array despite the larger number of junctions is emitting in a coherent superradiant manner.

The observed difference suggests that a nonresonant traveling-wave mechanism of synchronization contributes to the observed superradiant emission in the meander array, along with persisting standing-wave resonances. For the linear array standing waves are more prominent. However, a certain asymmetry of the radiation pattern indicates that the traveling wave may exist also in the linear array.

VI. CONCLUSIONS

In conclusion, we study electromagnetic wave emission from large Nb/NbSi/Nb Josephson-junction arrays with sizes significantly larger than emitted wavelengths. We observe that both arrays exhibit standing-wave resonances in current-voltage characteristics, but the emission maximum in the meander array does not occur at resonant conditions. Moreover, it shows nonlinear thresholdlike enhancement of the emission efficacy above a certain number of oscillating junctions, indicating the occurrence of the coherent superradiant emission. An analysis of the angular dependence of the emission for both samples reveals a forward-backward asymmetry of the radiation patterns, which is not expected for standing waves. We argue that the observed asymmetry provides evidence for the existence of a nonresonant mechanism of synchronization driven by the unidirectional traveling wave along the array. Our conclusion about the realization of a traveling-wave regime in Josephson-junction arrays is supported by numerical simulations for a Josephson traveling-wave antenna. We argue that this mechanism can help to synchronize very large arrays, in which the standing-wave mechanism of synchronization becomes inefficient. This is important for achieving superradiant power enhancement of very large arrays of oscillators of any type.

ACKNOWLEDGMENTS

[1] I. K. Yanson, V. M. Svistunov, and I. M. Dmitrenko, Experimental observation of the tunnel effect for cooper pairs with the emission of photons, Zh. Eksp. Teor. Fiz. **48**, 976 (1965) [, Sov. Phys. JETP **21**, 650 (1965)].

[2] V. P. Koshelets and S. V. Shitov, Integrated superconducting receivers, Supercond. Sci. Technol. **13**, R53 (2000).

[3] E. A. Borodianskyi and V. M. Krasnov, Josephson emission with frequency span 1–11 THz from small $Bi_2Sr_2CaCu_2O_{8+\delta}$ mesa structures, Nat. Commun. **8**, 1742 (2017).

[4] S. O. Katterwe, H. Motzkau, A. Rydh, and V. M. Krasnov, Coherent generation of phonon-polaritons in $Bi_2Sr_2CaCu_2O_{8+x}$ intrinsic Josephson junctions, Phys. Rev. B **83**, 100510(R) (2011).

[5] P. Barbara, A. B. Cawthorne, S. V. Shitov, and C. J. Lobb, Stimulated Emission and Amplification in Josephson Junction Arrays, Phys. Rev. Lett. **82**, 1963 (1999).

[6] U. Welp, K. Kadowaki, and R. Kleiner, Superconducting emitters of THz radiation, Nat. Photonics **7**, 702 (2013).

[7] F. Song, F. Müller, T. Scheller, A. Semenov, M. He, L. Fang, H. W. Hübers, and A. M. Klushin, Compact tunable sub-terahertz oscillators based on Josephson junctions, Appl. Phys. Lett. **98**, 142506 (2011).

[8] M. A. Galin, A. M. Klushin, V. V. Kurin, S. V. Seliverstov, M. I. Finkel, G. N. Goltsman, F. Müeller, T. Scheller, and A. D. Semenov, Towards local oscillators based on arrays of niobium Josephson junctions, Supercond. Sci. Technol. **28**, 055002 (2015).

[9] S. Han, B. Bi, W. Zhang, and J. E. Lukens, Demonstration of Josephson effect submillimeter wave sources with increased power, Appl. Phys. Lett. **64**, 1424 (1994).

[10] P. A. A. Booi and S. P. Benz, High power generation with distributed Josephson-junction arrays, Appl. Phys. Lett. **68**, 3799 (1996).

[11] S. Kiryu, W. Zhang, S. Han, S. Deus, and J. E. Lukens, Off-chip detection of radiation from a linear array oscillator with a spiral antenna, IEEE Trans. Appl. Supercond. **7**, 3107 (1997).

[12] L. Ozyuser, A. E. Koshelev, C. Kurter, N. Gopalsami, Q. Li, M. Tachiki, K. Kadowaki, T. Yamamoto, H. Minami, H. Yamaguchi, T. Tachiki, K. E. Gray, W.-K. Kwok, and U. Welp, Emission of coherent THz radiation from superconductors, Science **318**, 1291 (2007).

[13] T. M. Benseman, A. E. Koshelev, K. E. Gray, W.-K. Kwok, U. Welp, K. Kadowaki, M. Tachiki, and T. Yamamoto, Tunable terahertz emission from $Bi_2Sr_2CaCu_2O_{8+\delta}$ mesa devices, Phys. Rev. B **84**, 064523 (2011).

[14] S. Sekimoto, C. Watanabe, H. Minami, T. Yamamoto, T. Kashiwagi, R. A. Klemm, and K. Kadowaki, Continuous 30 μW terahertz source by a high-T_c superconductor mesa structure, Appl. Phys. Lett. **103**, 182601 (2013).

[15] T. Kashiwagi, T. Yamamoto, T. Kitamura, K. Asanuma, C. Watanabe, K. Nakade, T. Yasui, Y. Saiwai, Y. Shibano, H. Kubo, K. Sakamoto, T. Katsuragawa, M. Tsujimoto, K. Delfanazari, R. Yoshizaki, H. Minami, R. A. Klemm, and K. Kadowaki, Generation of electromagnetic waves from 0.3 to 1.6 terahertz with a high-T_c superconducting $Bi_2Sr_2CaCu_2O_{8+\delta}$ intrinsic Josephson junction emitter, Appl. Phys. Lett. **106**, 092601 (2015).

[16] V. M. Krasnov, Coherent flux-flow emission from stacked Josephson junctions: Nonlocal radiative boundary conditions and the role of geometrical resonances, Phys. Rev. B **82**, 134524 (2010).

[17] H. B. Wang, S. Guenon, J. Yuan, A. Iishi, S. Arisawa, T. Hatano, T. Yamashita, D. Koelle, and R. Kleiner, Hot Spots and Waves in $Bi_2Sr_2CaCu_2O_8$ Intrinsic Josephson Junction Stacks: A Study by Low Temperature Scanning Laser Microscopy, Phys. Rev. Lett. **102**, 017006 (2009).

[18] S. O. Katterwe and V. M. Krasnov, Temperature dependences of geometrical and velocity-matching resonances in $Bi_2Sr_2CaCu_2O_{8+x}$ intrinsic Josephson junctions, Phys. Rev. B **84**, 214519 (2011).

[19] V. V. Kurin, N. K. Vdovicheva, and I. A. Shereshevsky, Josephson traveling-wave antennas, Radiophys. Quantum Electron. **59**, 922 (2017).

[20] C. A. Balanis, in *Antenna Theory: Analysis and Design*, 3rd ed. (Wiley Interscience, New York, 2005), Chap. 10.

[21] A. A. Awad, P. Dürrenfeld, A. Houshang, M. Dvornik, E. Iacocca, R. K. Dumas, and J. Åkerman, Long-range mutual synchronization of spin Hall nano-oscillators, Nat. Phys. **13**, 292 (2017).

[22] F. Müller, R. Behr, T. Weimann, L. Palafox, D. Olaya, P. D. Dresselhaus, and S. P. Benz, 1 V and 10 V SNS programmable voltage standards for 70 GHz, IEEE Trans. Appl. Supercond. **19**, 981 (2009).

[23] A. N. Vystavkin, V. N. Gubankov, V. N. Listvin, and V. V. Migulin, Limit sensitivity of detectors based on electron gas heating in *n*-InSb, Izv. Vyssh. Uchebn. Zaved., Radiofiz. **11**, 602 (1968) [, Radiophys. Quantum Electron. **11**, 334 (1968)].

[24] We cannot exclude that a part of the complexity (fine structure) of measured radiation patterns may be caused by reflections from the cryostat walls because we did not take special precautions for dampening of such reflections. Therefore, not all of the fine structure may be important. The rotational stage is fully symmetric with respect to positive or negative angle rotation. Therefore, the observed forward-backward asymmetry of the radiation patterns is not caused by eventual reflections.

[25] K. S. Yee, Numerical solution of initial boundary value problems involving Maxwell's equations in isotropic media, IEEE Trans. Antennas Propag. **14**, 302 (1966).

[26] K. K. Likharev, in *Dynamics of Josephson Junctions and Circuits* (Gordon and Breach, New York, 1986), Chap. 1.

[27] R. Paschotta, in *Encyclopedia of Laser Physics and Technology* (Wiley-VCH, Weinheim, 2008), p. 403.

[28] J. Crank and P. Nicolson, A practical method for numerical evaluation of solutions of partial differential equations of the heat conduction type, Proc. Cambridge Philos. Soc. **43**, 50 (1947).

[29] A. Taflove and S. C. Hagness, in *Computational Electrodynamics: The Finite-Difference Time-Domain Method*, 3rd ed. (Artech House Inc., Boston and London, 2005), Chap. 8.

[30] J. P. Berenger, Three-dimensional perfectly matched layer for the absorption of electromagnetic waves, J. Comput. Phys. **127**, 363 (1996).

[31] V. V. Kurin, A. M. Klushin, I. A. Shereshevsky, and N. K. Vdovicheva, Simulation of Josephson antenna in 3D space, in *Proceedings of the International Conference Days on Diffraction 2016* (St. Petersburg, Russia, 2016), pp. 259–263.

[32] G. Filatrella, N. F. Pedersen, C. J. Lobb, and P. Barbara, Synchronization of underdamped Josephson-junction arrays, Eur. Phys. J. B **34**, 3 (2003).